Mineral-catalyzed formation of marine NO and N₂O
on the anoxic early Earth

Steffen Buessecker[1][§][*], Hiroshi Imanaka[2,3], Tucker Ely[4], Renyu Hu[5,6], Stephen J. Romaniello[4,7], Hinsby Cadillo-Quiroz[1,8]

[1] School of Life Sciences, Arizona State University, Tempe, AZ, USA.

[2] SETI Institute, Mountain View, CA, USA.

[3] NASA Ames Research Center, Moffett Field, CA, USA.

[4] School of Earth and Space Exploration, Arizona State University, Tempe, AZ, USA.

[5] Jet Propulsion Laboratory, California Institute of Technology, Pasadena, CA, USA.

[6] Division of Geological and Planetary Sciences, California Institute of Technology, Pasadena, CA, USA.

[7] Department of Earth and Planetary Sciences, University of Tennessee, Knoxville, TN, USA.

[8] Biodesign Institute, Arizona State University, Tempe, AZ, USA.

[§] Current address: Department of Earth System Science, Stanford University, Stanford, CA, USA.

[*] Correspondence to: S. Buessecker (sbuessecker@stanford.edu)

Abstract

Microbial denitrification converts fixed nitrogen species into gases in extant oceans. However, it is unclear how such transformations occurred within the early nitrogen cycle of the Archean. Here we present experimental anoxic surface-catalyzed reduction of nitrite and nitrate via green rust and magnetite combined with diffusion and photochemical modeling. We find that in a Fe^{2+}-rich marine environment, Fe minerals could have catalyzed abiotic denitrification reactions leading to the formation of nitric oxide (NO) and nitrous oxide (N_2O). Nitrate did not exhibit reactivity in the presence of either mineral or aqueous Fe^{2+}, however, both minerals induced rapid nitrite reduction to NO and N_2O. While N_2O escaped into the atmosphere (63% of nitrite-nitrogen, with green rust as catalyst), NO remained associated with precipitates (7%) serving as a potential shuttle to the benthic ocean. The modeling suggests that marine N_2O emissions would have sustained 0.8-6 ppb of atmospheric N_2O without a protective ozone layer. Our findings add detail to the as yet incompletely documented Archean nitrogen cycle, implying a globally distributed process driven by chemical kinetics similar to those of modern enzymatically mediated conversions.

Prior to the rise of O_2 during the Great Oxidation Event (GOE), the Archean ocean

20   received oxides of nitrogen (NO_x) by deposition of abiotic nitrogen fixation products[1]. As a

consequence, nitrite (NO_2^-) and nitrate (NO_3^-) reached seawater concentrations in the lower µM

range[1-4]. While microbial denitrification plays a dominant role in modern oceans to recycle NO_x^-

into gaseous phases, such pathways were not available in the Archean without active NO_x^-

reductases. A non-enzymatic process reducing fixed NO_x^- into gases is chemodenitrification,

25   which is of particular interest because nitrous oxide (N_2O) can be a primary product[5-7]. The

Archean atmosphere prior to the GOE was likely dominated by N_2 and CO_2, with ppm-levels of

CO, CH_4, and H_2 (ref. [8]). The introduction of even trace amounts of more oxidized gases, such as

N_2O, could have created a significant source of thermodynamic disequilibrium to drive primitive

ecosystems. Further, N_2O is a strong greenhouse gas and has been considered to induce a warmer

30   climate under a faint young Sun[9]. Stanton *et al.* first showed through experiments and modeling

that aqueous Fe^{2+} could have acted as a driver for chemodenitrification to form N_2O abiotically in

Proterozoic oceans[10]. Yet, N_2O production rates established for the early marine environment, thus

far, have been ~4 orders of magnitude lower than rates reported from isotope tracer measurements

in modern oxygen minimum zones (Table 1), underlining the catalytic importance of

35   denitrification enzymes for rapid nitrogen cycling. As a result, it has been hypothesized that N_2O

was virtually absent on the anoxic early Earth, especially without a protective ozone (O_3) layer to

compensate for elevated photolytic N_2O destruction[11-13]. While under ferruginous conditions

aqueous Fe^{2+} has not stimulated N_2O production close to microbially mediated rates (Table 1),

mineral phases bear the potential to reach such rates and could have therefore provided efficient

40   pathways to channel fixed nitrogen back into the Archean atmosphere.

Here, we evaluated the role of the mineral-catalyzed formation of NO and N_2O as a

marine source pathway under anoxic, ferruginous conditions. NO has been measured in mixtures

of NO_x^- and highly concentrated Fe^{2+} solutions[5] and in a MoS_2 suspension under a geoelectric

current[14], but it has only been speculated to be produced in Fe mineral suspensions[6,7]. The ferrous-

45   ferric hydroxy salt carbonate green rust (GR, $[Fe^{2+}_{(1-x)} Fe^{3+}_x (OH)_2]^{x+} \cdot [(x/2)CO_3^{2-} \cdot (m/2)H_2O]^{x-}$)

has been shown to precipitate from Archean seawater-analog solutions, consistent with

thermodynamics predicting a predominance of GR in the Fe sink fraction along the water column

prior to 2.5-2.7 Ga[15]. Settling GR particles could have provided a transport mechanism for trace

compounds to the seafloor[15], where reducing conditions partially converted GR to magnetite

50   (Fe_3O_4), an important constituent of banded iron formations. Because NO_2^- and NO_3^- can

spontaneously react in presence of reduced Fe[16-18], we tested the reactivity of the mixed-valence Fe

minerals GR and magnetite with NO_2^- and NO_3^- at *low* (1-5 μM), *high* (20-35 μM), and *excessive*

(200-350 μM) abundances, and characterized their potential to produce NO and N_2O at relevant

rates for the Archean ocean-atmosphere system. To do so, we used mineral particle concentrations

55   recorded for modern analogues as a proxy for mineral abundance (*Supplementary Figs. 1-4*). We

experimentally simulated ferruginous conditions with a simple end-member artificial seawater

recipe using a 20% CO_2-HCO_3^- buffer devoid of sulfur. Subsequent flux and photochemical

calculations suggest marine mineral-catalyzed NO and N_2O formation constituted a substantial

source of gaseous nitrogen oxides on the anoxic early Earth.

60

\<Table 1\>

4

Abiotic NO_x^- reduction under simulated Archean conditions

We first compared the reactivity of NO_3^- and NO_2^- with GR, magnetite and aqueous Fe^{2+} separately. For all reductants, consumption of NO_3^- and production of N_2O was negligible (<0.03 nmol h^{-1}, Fig. 1a) even over a prolonged period of 100 days. In contrast, NO_2^- showed reactivity in the presence of both mineral catalysts, and was stable in controls with 500 μM aqueous Fe^{2+}. The

70   contrasting reactivity of the nitrogen oxides is reflected in the solid phase Fe^{2+}/Fe^{3+} ratio determined at the end of the experiment (Fig. 2), revealing a trend of higher mineral oxidation with increasing NO_2^- concentration. Magnetite and GR showed disparate potential to produce N_2O. Concomitant with a more rapid NO_2^- consumption, N_2O production rates were more than 10 times higher when GR was the catalyst (Fig. 1b). At GR surface areas observed for the Archean ocean

75   analogue Lake Matano, Indonesia[29] (~10^{-3} m^2 mL^{-1}, Fig. 1c, d), abiotic N_2O production rates were highly similar to (*low* NO_2^-) or exceeding (*high* NO_2^-) biotic production rates measured recently in the Eastern Tropical North Pacific[19,20] (Table 1). As a reference, modern NO_2^- concentrations are near the bottom of the experimental range employed here, which extends higher to account for a range of possible Archean NO_x^- abundances (see discussion below).

80

<Fig. 1>

The conversion of NO_2^- to N_2O was not equimolarily balanced and we therefore considered accumulation of NO as intermediary species[30]. After initially observing modest NO

85   accumulation, we injected concentrated hydrochloric acid in order to dissolve mineral particles and release any nitrogen bound to mineral surfaces. Indeed, the particle dissolution was followed by a spike in headspace NO (Fig. 1e). At least 92% of the total NO was bound to GR (97% was bound to magnetite). To rule out reaction of the acid with residual NO_2^-, we conducted controls with

sulfuric acid and NO_2^- (*Supplementary Table 3*). Other controls evaluating the stability of NO in

90   the mineral suspension included acid injection at later time points in time-extended experiments.

NO yields at 220 hours (< 0.5 μM NO_2^-) were similar to those at 50 hours after NO_2^- addition

(*Supplementary Fig. 5, Supplementary Table 3*). We calculated the NO yield in respect to the total

NO_2^- and, accordingly, 7% reacted to NO (over 63% that reacted to N_2O) with GR as catalyst and

87% reacted to NO (over 8% that reacted to N_2O) with magnetite as catalyst. The remaining

95   product pool could be N_2 (ref. [30]) and only constituted a minor fraction. Our data show that

mineral-associated NO, presumably in the form of nitrosyl species[31], is a significant byproduct and

geochemically stable in presence of Fe mineral phases.

<Fig. 2>

100

N₂O accumulation triggered by marine emissions

To elucidate the impact of the experimentally derived production rates on N_2O dispersion

in seawater and emission to the Archean atmosphere, we combined diffusion models into a simple

flux balance model (*Supplementary Information*). We considered a 100 m deep ocean slab beneath

105   the photic zone as the part of the water column with a maximum overlap of NO_x^- ions from the

surface and GR formation fueled by upwelling Fe^{2+}-rich water from the depth. An estimate of the

GR particle concentration in the Archean ocean was informed by observed Fe particle numbers

from seven modern marine and freshwater anoxic basins (Fig. 1d), including Kabuno Bay (KB),

East Africa[32]. The peak Fe^{2+} concentration in the particulate fraction of KB waters (11 μM) closely

110   reflects concentrations used for the thermodynamic modeling of GR precipitation in Archean

seawater[15], which is why we used the KB level as reference and enveloped that value with a

putative lower and upper boundary of 50% and 500%. Archean seawater Fe^{2+} could have reached

concentrations of 55 µM, as constrained by Fe^{2+} toxicities on cyanobacteria[33] and the appearance of herringbone and micritic carbonates[34,35]. At that upper boundary and under *low* (conservative)

115 NO_2^- conditions, net N_2O emissions conceivably reached 235 [98.1–413.9] nmol m^{-2} h^{-1} (95% CI, *Supplementary Figs. 6 and 7*, *Supplementary Table 4*), implicating 4 times the modern marine average flux[36]. Overall, N_2O emissions from the ferruginous ocean gradually increased with the GR particle concentration.

120   To simulate the effect of N_2O fluxes triggered by mineral catalysis into an anoxic Archean atmosphere, we applied a photochemical model[37]. We probed four different N_2O fluxes corresponding to *low* and *high* NO_2^- levels and Fe^{2+} concentrations in GR phases around the KB reference (*Supplementary Table 4*). Although the upper boundary of our estimates implicates near-modern N_2O abundances in the troposphere (0-13 km altitude, Fig. 3), N_2O concentrations derived

125 from *low* NO_2^- seawater levels, and predicted to be 0.8-6 ppb, are more realistic. These concentrations match mixing ratios in previous Proterozoic atmosphere models assuming 1% of present O_2 levels[10,13]. A striking difference is, however, the inclusion of an O_3 protective layer in previous models, which was assumed to be present after the GOE, i.e. in the Proterozoic. Our photochemical model produced an ozone column of ~9.6×10^{14} molecules cm^{-2}, which is less than

130 the present-day level by 4 orders of magnitude and previously modeled Proterozoic levels by ~3 orders of magnitude. Thus, without the aid of O_3 shielding, marine mineral-catalyzed N_2O production generated tropospheric N_2O levels akin those in oxygenated atmospheres later in Earth's history.

135 **<Fig. 3>**

The main sink of N_2O is photolysis by radiation <230 nm[40] in the stratosphere, which

governs the shape of the concentration profiles (Fig. 3a). In the Archean atmosphere, N_2O

abundances could have been higher due to i) additional sources and ii) protective agents against

140 UV light. For instance, high-energy particles from solar flares led to N_2O formation most active at

higher altitudes and could complement surface sources[41]. These pathways were perhaps more

pronounced in the Hadean or early Archean when the Sun was more active and the magnetic field

openings were greater at the poles. Furthermore, in the presence of methane hazes, N_2O could have

been shielded through strong UV absorption by fractal haze particles[39], which prolonged its

145 lifetime. A sensitivity study using the photochemical model shows that, with a fractal haze, N_2O

concentrations derived from *low* NO_2^- seawater levels can build up to 1-7 times the present-day

atmospheric level (Fig. 3b). One may ask if this buildup of abiotic N_2O may constitute a "false

positive" scenario for using N_2O as a biosignature gas for terrestrial exoplanets akin to the Archean

Earth. We suggest that this would not be a true false positive because the high abundance of

150 methane, which is the prerequisite of the fractal haze layer, is likely biogenic in the first place.

Despite the extent of tropospheric N_2O predicted by our model, effects on the planetary

climate were probably modest because N_2O would not be sufficiently concentrated to significantly

increase the infrared atmospheric opacity in CO_2 window regions. Especially in high CO_2

155 atmospheres, the N_2O radiative forcing is diminished since it may not occupy otherwise

transparent infrared windows. The infrared window between 6 and 8 μm could potentially be filled

by N_2O absorption, but this is dependent on atmospheric methane which absorbs at similar

wavelengths[13]. Since methane concentrations were likely >100 ppmv[42], greenhouse warming by

N_2O under our simulated conditions therefore contributed only weakly to a warmer climate under

160   the faint young Sun of the Archean[9].

Fe mineral reactions as significant sink for marine NO_x^-

Because of prevailing ferruginous conditions, mineral reactions were likely limited by

abiotic nitrogen fixation rates rather than mineral surface area. Previous seawater NO_x^- estimations

165   (8.7-24,000 μM^2, 1-10,000 μM^{43}, <1 μM^4 and 0.2-2 μM^{38}) contain a large uncertainty. For

comparison, modern NO_2^- concentrations reach ~1.5 μM around oxygen minimum zones, but

contrary to the Archean ocean, oxidoreductases effectively suppress NO_2^- accumulation[44]. While

previous estimates refer to the average bulk seawater composition, top-down gradients of NO_x^- or

conical zones of higher NO_x^- concentrations beneath rainout areas contributed perhaps to a more

170   heterogeneous distribution. In such zones, NO_x^- may have reached steady-state concentrations well

above the *low* NO_x^- range (1-5 μM) designated here.

Our experimental data suggest rapid consumption of seawater NO_x^- (NO_2^- in particular)

revealing a sink distributed over the pelagic ocean that has thus far not been accounted for.

175   Previously proposed geochemical reactions that consumed dissolved NO_x^- species on the early

Earth included reduction to ammonia[45] and reduction of NO_3^-, NO_2^- and N_2 during water-rock

interactions between hydrothermal fluids and the oceanic crust[46-48]. However, abiotic NO_x^-

conversion to ammonia is not significant at pH $\leq$ 7.3 (ref. [45]), a regime that dominated the early

oceans[49], and therefore restricted this NO_x^- sink to more alkaline environments, such as ultramafic-

180   hosted hydrothermal vents. Because NO_3^- was photo-reduced to NO_2^- and mineral-catalyzed

reduction of NO_2^- is several orders of magnitude faster than photo-reduction of NO_2^- (ref. [4]),

9

reaction on Fe mineral surfaces constituted a sink for fixed nitrogen from both the NO_3^- and NO_2^- pool. We henceforth tested if NO_2^- consumption on mineral particles and in sediments exhausted seawater NO_2^-, possibly impeding mineral-catalyzed NO and N_2O production (*Supplementary*

185 *Information*). Assuming a combined NO_x flux of 2.5×10^{11} mol N yr^{-1} from lightning events[50], volcanic eruptions[51], and meteoritic impacts[52], GR particle surfaces equivalent to 200% KB draw NO_2^- concentration down to 8.4 µM. At higher GR abundances, the reactants became exhausted and any NO_2^- from NO_3^- photo-reduction or deposited to the ocean directly converted to NO and N_2O. Importantly, abiotic fluxes were co-regulated by the influx of NO_x into the ocean and the

190 amount of GR suspended in seawater. If N_2O formation dropped due to reactant limitation, atmospheric N_2O may have reached sub-ppb concentrations, but no lower than HNO-derived N_2O concentrations (>0.5 ppb, Fig. 3).

Effects of NO and N_2O on early anaerobic microbial life

195   With the assumption that individual denitrification steps evolved consecutively, our results provide a geochemical explanation for biochemical patterns known for over three decades. A primitive form of NO and N_2O reduction likely preceded aerobic respiration based on the structural resemblance of NO[53] and N_2O[54-56] reductases (Nor and Nos) with components of cytochrome c oxidase, including hydrogen-bond- and metal-configuration, Ca ligation[57], and

200 phylogenetic analyses[53,58]. This concept is supported by a simple make-up of the respiratory chains involving quinone-dependent Nor and membrane-bound Nos, as present in some gram(+) bacteria[55,56]. Because of their dependence on a complex cytochrome c maturation system, NO_3^- and NO_2^- reductases probably evolved later[59].

In order to constrain the effects of N_2O on early microorganisms, we estimated dissolved

205   abundances based on atmosphere-to-seawater diffusion. Accordingly, at least 0.04-4.7 nM N_2O

were dissolved in the ferruginous seawater based on mere equilibration with the Archean air

without haze (*Supplementary Table 4*). True concentrations were likely higher in proximity around

actively N_2O-generating GR particles. Contemporary microbial N_2O consumption is based on

high-affinity enzymes adapted to low N_2O steady-state concentrations[60]. For example, 30 nM N_2O

210   is readily metabolized in anoxic seawater[61], but the critical threshold for marine N_2O respiration is

likely much lower (pers. commun., Sukhwan Yoon, KAIST).

<Fig. 4>

215   Under generally accepted Archean ocean conditions, N_2O reduction to N_2 is

thermodynamically favorable but kinetically hindered without enzymatic catalysis, making it an

ideal potential energy source. For instance, coupled to H_2 oxidation (H_2 as a simple and available

reductant), an affinity of up to 300 kcal per electron accepted by N_2O is significantly higher than

that of any other redox reaction tested. Moreover, GR-shuttling may have been effective for NO

220   molecules to reach benthic microbial life, acting as a biological electron sink[53]. The availability of

NO was essential for early denitrifying microorganisms because marine sediments in the Archean

lacked nitrification as source of NO_x. The reduction of the available NO_x (Fig. 4a-c) achieves a

higher energy yield than magnetite reduction (Fig. 4d) and methanogenesis (Fig. 4e), underscoring

their benefit to microbial life in a sulfate-poor marine environment.

225   Conversely, NO and N_2O could have been damaging to microorganisms. The inhibitory

effects of the NO molecule are caused by radical production and nitrosative stress[62], which forced

microbial cells to rapidly reduce NO using Nor-type enzymes. Given the negative effects of NO on phototrophs[63,64] (15 nM NO halted growth), mineral-catalyzed NO formation could have corrupted the capability of phototrophic communities to harvest light energy. In contrast to its energetic

230   benefits, N_2O can bind and inactivate vitamin B_{12}[65,66]. Among diverse roles as cofactor in essential cellular processes, vitamin B_{12} is a key metabolite for methanogens because its cobalt(I) center serves as a methyl acceptor during methanol to methane transformation[67]. For example, methanogens in tropical soils have shown metabolic sensitivity to N_2O as low as 4 nM[68] which could have feasibly accumulated in ferruginous waters (*Supplementary Table 4*). Whether NO and

235   N_2O had positive or negative net effects on early microorganisms remains elusive but, in either case, a mineral source of these compounds inevitably exerted selective pressure and shaped the composition of Archean microbial communities.

Our study suggests that a significant portion of NO_x^- in the ferruginous Archean ocean was diverted to NO and N_2O leading to more oxidized products compared to other sink pathways

240   (ending in N_2 or ammonia). Given GR phases at 100% KB equivalence, *low* seawater NO_2^- levels, and a 70% ocean cover of Earth's surface, N_2O emissions exported 2.1 Tg N yr^{-1} into the Archean atmosphere. We regard any biological N_2O production (e.g., through ammonia oxidation) that would have added to this flux as insignificant in the reducing milieu of a ferruginous ocean. Considerable amounts of mineral surface-bound NO could have been transported down to the

245   seafloor by settling of GR precipitates. Assuming a particle sinking velocity of 50 m day^{-1} (ref. [69]), 1.2 Tg N yr^{-1} in the form of NO could have reached ocean sediments. Thus, the degree of thermodynamic disequilibria in the redox balance of the Archean nitrogen cycle may have been underestimated[70]. We also caution to use N_2O as unique biosignature in exoplanet exploration. It is possible that conditions for the mineral-catalyzed N_2O production on early Earth-like exoplanets

250 are even more favorable, resulting in N_2O atmospheric concentrations exceeding modern ones

(higher abiotic nitrogen fixation rates, higher Fe mineral load). Signals from low-methane

atmospheres could be interpreted as false positives without any biological basis.

<Fig. 5>
255

We provide evidence that higher O_3 levels are not required to reach ppb N_2O

concentrations prior to the GOE and present a concept of a complete abiotic N_2O cycle closed by

mineral-catalyzed reactions (Fig. 5), hundreds of millions of years prior to the biological and more

efficient production and consumption of N_2O[11]. Although the effects of abiotic N_2O production

260 were probably modest on the early climate, marine sources of NO and N_2O could have markedly

influenced the evolution and survival strategies of Archean life. Rather than being a mainly

biological invention, the reduced branch of the abiotic nitrogen cycle, driven by chemical kinetics

highly similar to those of modern enzymatically mediated conversions (Table 1), was seemingly

co-opted by early organisms.

265

270

Acknowledgments

Author Contributions

S.B., H.I. and H.C.-Q. developed the overall study objectives and the experimental design. S.B. performed the experiments. S.B., T.E. and S.R. conducted thermodynamic and diffusion modeling. R.H. created the photochemical model. S.B. and H.C.-Q. drafted the manuscript. All authors participated in final revisions of the paper.

Competing Interest

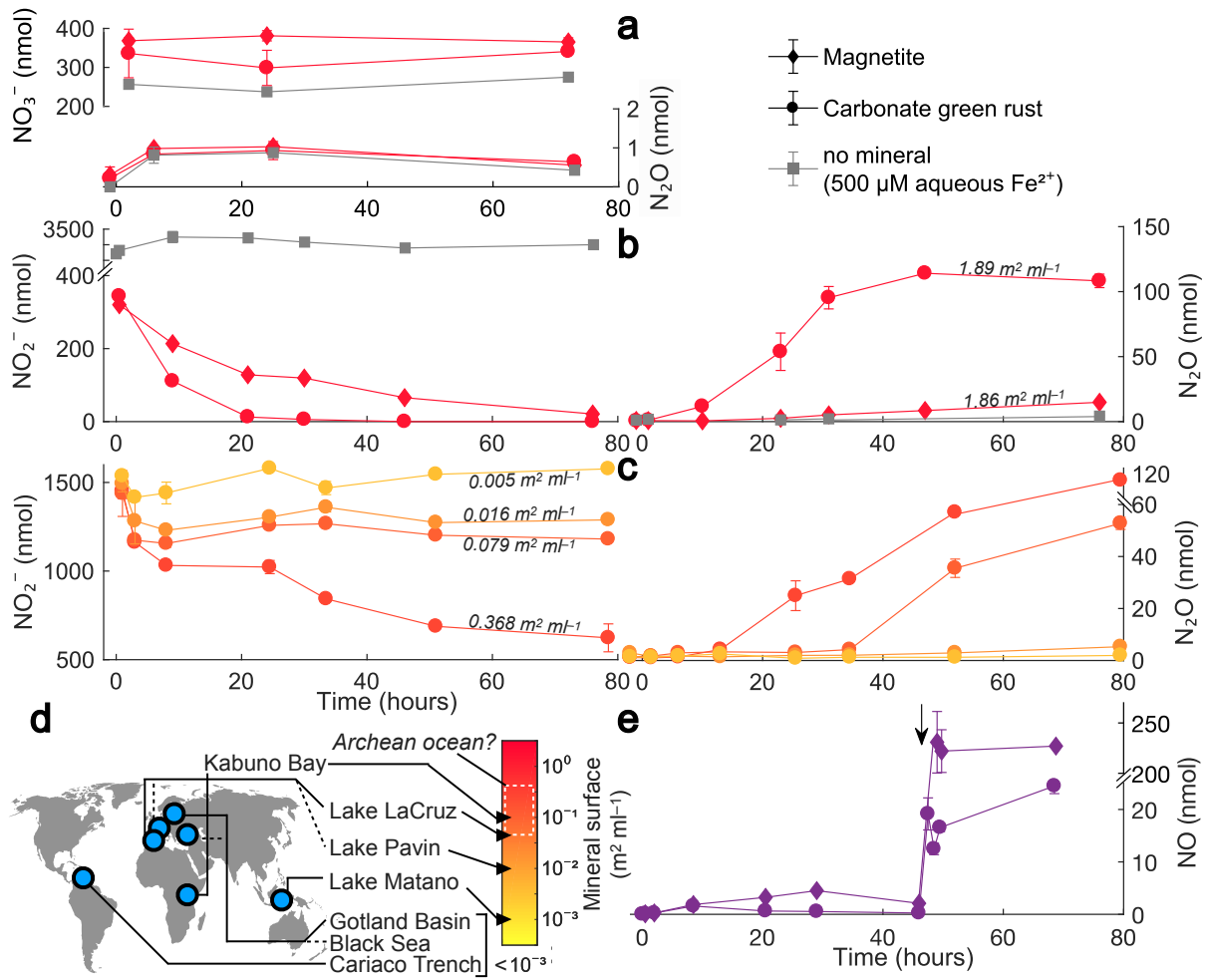The authors have no competing interests to declare.

14

Tables

Table 1. N_2O and NO production rates of the modern and early marine environment and from cultured microbial species.

Earth period	System	N_2O production rates (nM days^{-1})	Reference
modern	Eastern Tropical North Pacific	0.5-5	[19,20]
modern	Arabian Sea	0.005-0.08	[21]
modern	Eastern Tropical South Pacific	6-43.2	[22]
modern	Eastern Tropical North Atlantic	1.5-3.5	[23]
modern	Peruvian coastal upwelling zone	5-49	[24]
modern	cultured *Nitrosomonas marina* C-113a	2-3	[25]
modern	cultured *Nitrosomonas marina* NM22	1.4-4.2	[23]
modern	cultured *Nitrosococcus oceani* NC10	1.2-3.7	[23]
modern	cultured *Nitrosopumilus maritimus* SCM1	0.4-24.3	[23]
early	simulated ferruginous ocean with aqueous Fe^{2+}	0.0001-0.01	[10]
early	simulated ferruginous ocean with GR particles	0.3-17.9*	this study

Earth period	System	NO production rates (nM days^{-1})	Reference
modern	Equatorial Pacific, near 170° West	34.6-103.7	[26]
modern	Yellow Sea	129.6	[27]
modern	cultured *Nitrosopumilus maritimus* SCM1	4,800	[28]
early	simulated ferruginous ocean with GR particles	≥737.5**	this study

*Derived from incubations with *low* NO_2^- abundances and 0.005-0.366 m^2 ml^{-1} green rust surface. **Estimate of total (free and mineral-associated) NO based on particle dissolution after 50 hours in incubations with *high* NO_2^- abundances.
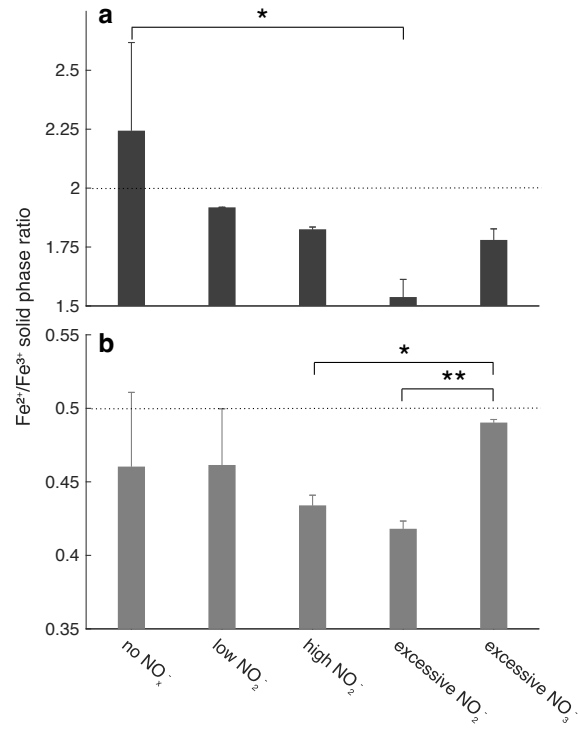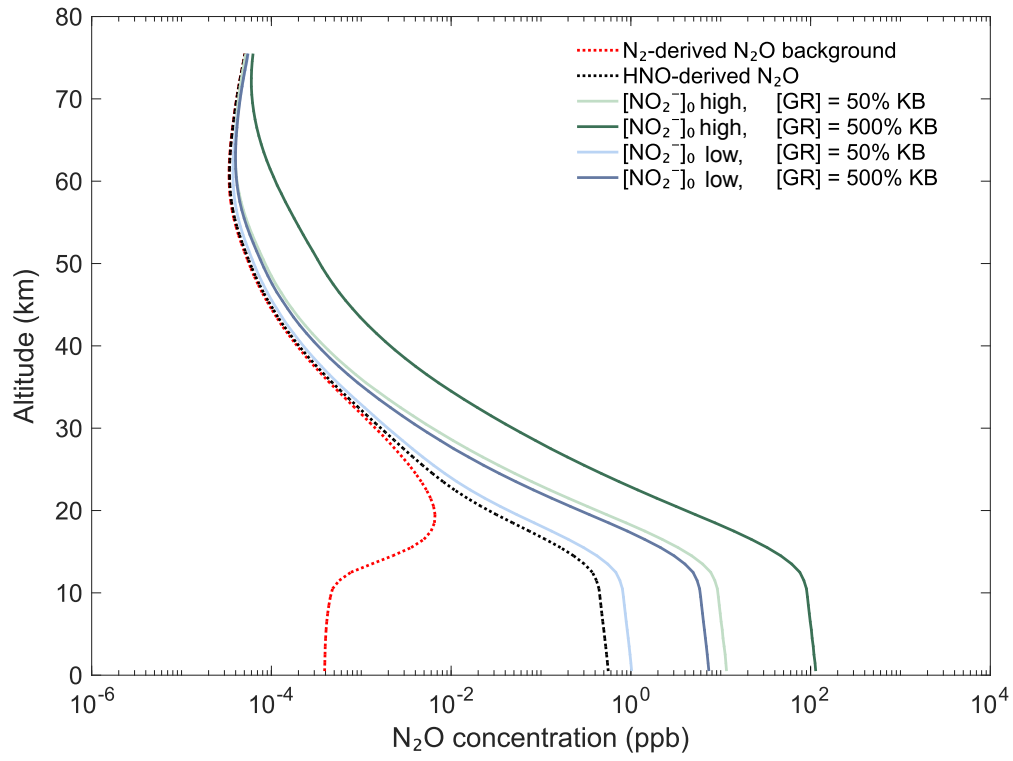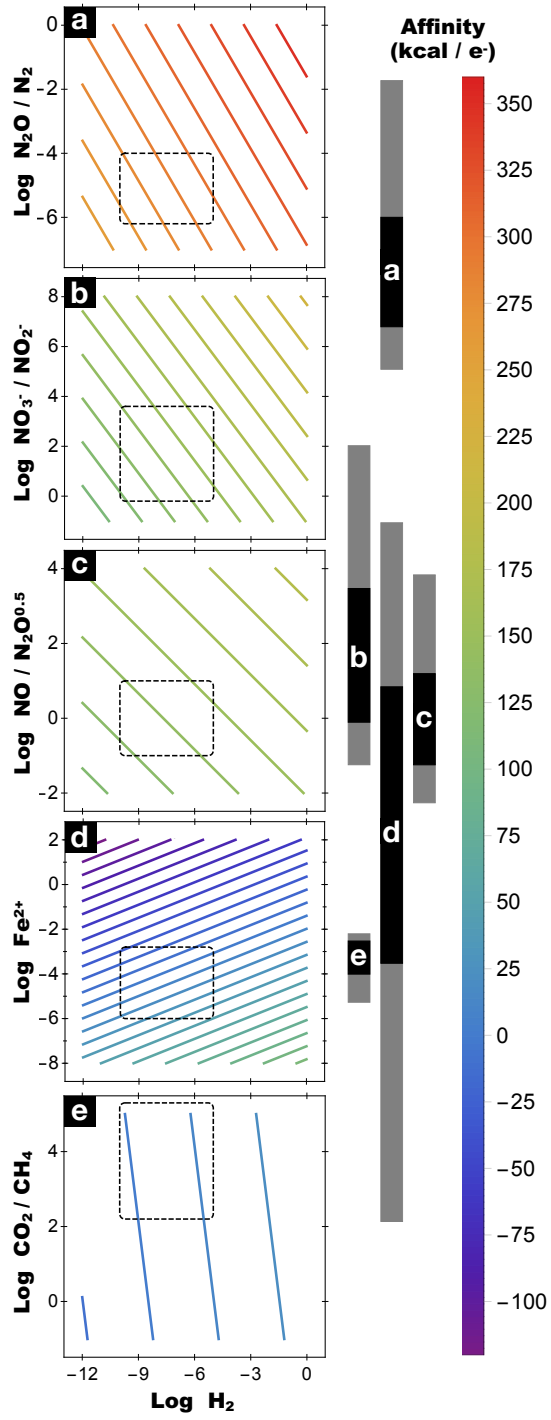
Figure
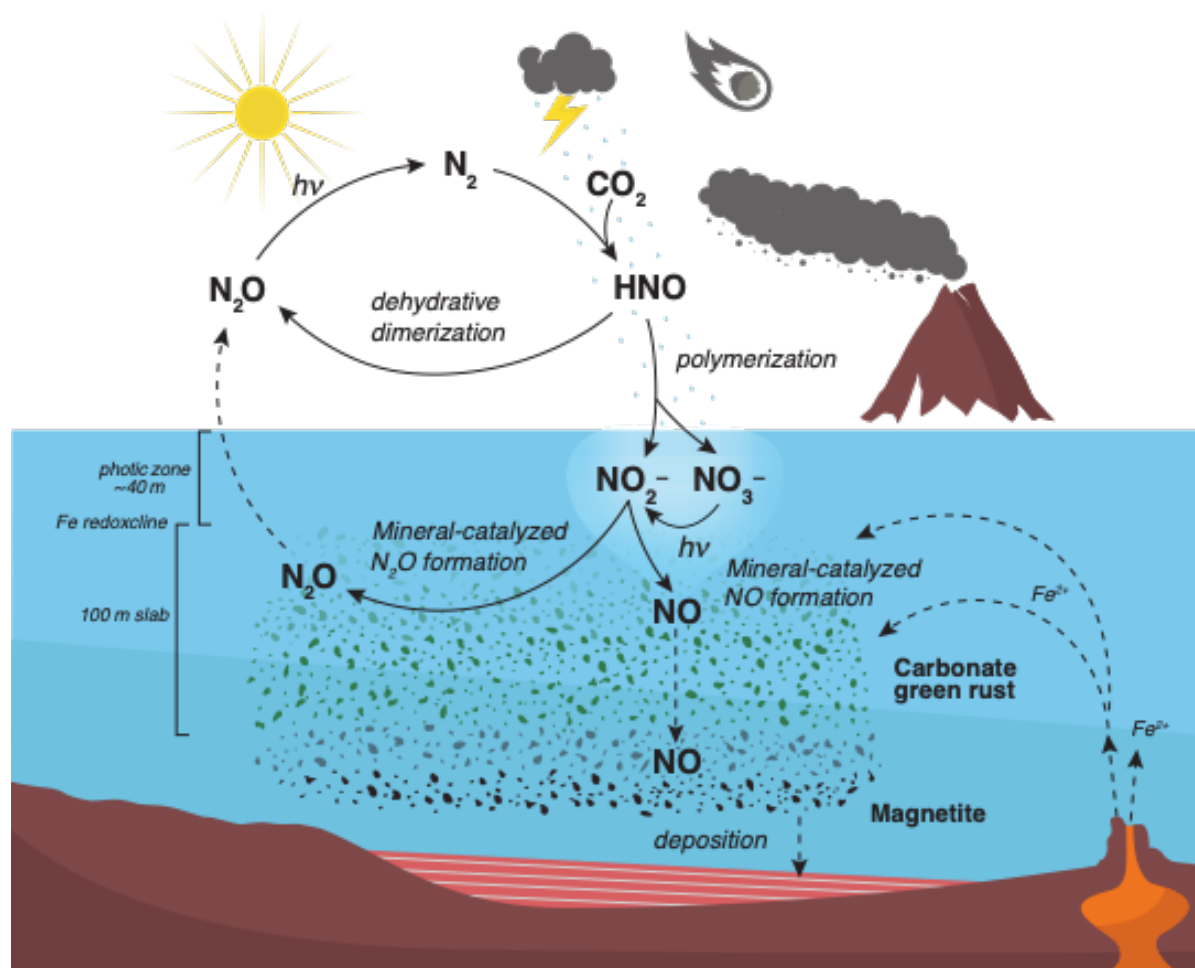
Fig. 2

320

Fig. 3

Fig. 4

Fig. 5

330

Figure Legends/Captions

Fig. 1. Molecular NO_x^- consumption and associated NO and N_2O production with Fe minerals or aqueous Fe^{2+}. Dissolved NO_3^- and NO_2^- in anoxic artificial seawater solution were
335   quantified concomitantly to NO and N_2O in the headspace. The results from incubations with initial NO_x^- concentrations in the *high* (20-35 µM) range are shown (all incubation results in *Supplementary Table 1*). Y-axes depict total quantities (gas + liquid phase) and are sometimes interrupted by breaks to better illustrate changes. **a**, NO_3^- amended microcosms with GR and magnetite. **b**, NO_2^- amended microcosms with GR and magnetite. **c**, NO_2^- reduction and N_2O
340   production under varying GR mineral surface. After initial rapid NO_2^- consumption, the reaction may become mineral surface-limited hindering the reduction of more NO_2^-. **d**, Range of GR surface area was informed by naturally occurring Fe mineral particles in modern Archean ocean analogues (*Supplementary Information*). **e**, NO formation with 33 µM initial NO_2^-, mineral surface identical to **b**. Arrow indicates addition of concentrated hydrochloric acid resulting in subsequent
345   mineral particle dissolution and outgassing of NO. Data are presented as mean values +/– *SD* (n = 3).

Fig. 2. Solid phase ratio of reduced and oxidized Fe in GR (a) and magnetite (b). Data were collected after acid digestion at the end of incubations. The dotted lines indicate stoichiometric GR
350   and magnetite, respectively. For total Fe abundances, see *Supplementary Table 2*. *P = 0.02, **P = 0.006, two-sided Student's t test. Columns indicate mean values and error bars denote one *SD* based on n = 2 (a) and n = 3 (b).

Fig. 3. Atmospheric N$_2$O under influence of mineral-catalyzed N$_2$O production in the Archean ocean. a, Abundances are based on fluxes assuming GR phases in KB equivalents with *low* and *high* seawater NO$_2^-$ levels. Background N$_2$O formation occurred via the reaction N$_2$ + O(^{1}D) + M → N$_2$O + M and O(^{1}D) was produced by photodissociation of CO$_2$ with photons more energetic than 167 nm. N$_2$O can also be derived directly through dehydrative dimerization of HNO that did not polymerize into NO$_3^-$ or NO$_2^-$ (ref. [38]). N$_2$O profiles do not account for N$_2$O from the HNO pathway. **b**, Atmospheric N$_2$O abundances when a fractal haze layer is included in the photochemical model. We adopt the fractal haze predicted by ref. [39] for the Archean atmosphere, which has an optical depth of ~10 at 200 nm and only ~0.6 at 500 nm. Bars at the right illustrate relative haze absorption based on data from ref. [39]. N$_2$O builds up to much higher abundances because of the strong shielding effect of haze.

Fig. 4. Affinity landscapes. a, Reduction of N$_2$O gas by molecular hydrogen (H$_2$). **b**, Reduction of NO$_3^-$ by H$_2$. **c**, Reduction of NO by H$_2$. **d**, Magnetite reduction by H$_2$ at pH 7.3. **e**, CO$_2$ reduction by H$_2$ (methanogenesis). The colored curves in each plot represent lines of constant affinity, set 10 kcal apart. Black boxes represent regions of likely species activities; i.e., each of these regions is aligned on the scale bar to the right for easier comparison between reactions. More detail to the reaction stoichiometry in the *Supplementary Information*.

Fig. 5. Schematic depiction of mineral-catalyzed NO and N$_2$O formation at the junction of the early nitrogen and iron cycle. Heat shock reactions, as stimulated by galactic cosmic rays, meteoritic impact plumes, volcanic and thunderstorm lightening, produced the central precursor HNO, which dimerized directly to N$_2$O or polymerized into NO$_2^-$ and NO$_3^-$ (ref. [38]). These nitrogen oxides became interspersed into the surface ocean as plumes by rainout. Any NO$_3^-$ constituted a source of NO$_2^-$ through photo-reduction[4]. Upwelling Fe^{2+} precipitated into Fe oxyhydroxides and GR in the Fe redoxcline. Driven by Fe mineral phases, NO$_2^-$ was reduced to N$_2$O. The abiotic nitrogen cycle was closed by photolytic destruction of emitted N$_2$O to N$_2$. As a byproduct, NO molecules remained bound at mineral particles as nitrosyl. This way, GR may have served as NO shuttle enabling transport into the deep ocean. Sinking GR transformed into Fe^{2+} carbonates, Fe^{2+} silicates, and magnetite, which then were deposited. Dashed lines mark diffusive or gravitational transport, whereas solid lines indicate chemical reactions.

390 **References**

1. Mancinelli, R. L. & McKay, C. P. The evolution of nitrogen cycling. *Orig Life Evol Biosph* **18,** 311–325 (1988).
2. Wong, M. L., Charnay, B. D., Gao, P., Yung, Y. L. & Russell, M. J. Nitrogen oxides in early Earth's atmosphere as electron acceptors for life's emergence. *Astrobiology* **17,** 975–
395 983 (2017).
3. Summers, D. P. & Khare, B. Nitrogen fixation on early Mars and other terrestrial planets: Experimental demonstration of abiotic fixation reactions to nitrite and nitrate. **7,** 333–341 (2007).
4. Ranjan, S., Todd, Z. R., Rimmer, P. B., Sasselov, D. D. & Babbin, A. R. Nitrogen oxide
400 concentrations in natural waters on early Earth. *Geochemistry, Geophys. Geosystems* **20,** 2021–2039 (2019).
5. Kampschreur, M. J., Kleerebezem, R., Vet, W. W. J. M. de & Loosdrecht, M. C. M. V. Reduced iron induced nitric oxide and nitrous oxide emission. *Water Research* **45,** 5945–5952 (2011).
405 6. Jones, L. C., Peters, B., Pacheco, J. S. L., Casciotti, K. L. & Fendorf, S. Stable isotopes and iron oxide mineral products as markers of chemodenitrification. *Environ. Sci. Technol.* **49,** 3444–3452 (2015).
7. Grabb, K. C., Buchwald, C., Hansel, C. M. & Wankel, S. D. A dual nitrite isotopic investigation of chemodenitrification by mineral-associated Fe(II) and its production of
410 nitrous oxide. *Geochim. Cosmochim. Acta* **196,** 388–402 (2017).
8. Kasting, J. F. Atmospheric composition of Hadean – early Archean Earth: The importance of CO. *Geol. Soc. Am.* 19–28 (2014). doi:doi:10.1130/2014.2504(04)
9. Gough, D. O. in *Physics of solar variations* 21–34 (Springer Dordrecht, 1981). doi:10.1007/978-94-010-9633-1_4
415 10. Stanton, C. L. *et al.* Nitrous oxide from chemodenitrification: A possible missing link in the Proterozoic greenhouse and the evolution of aerobic respiration. *Geobiology* **16,** 597–609 (2018).
11. Buick, R. Did the Proterozoic 'Canfield Ocean'cause a laughing gas greenhouse? *Geobiology* **5,** 97–100 (2007).
420 12. Godfrey, L. V. & Falkowski, P. G. The cycling and redox state of nitrogen in the Archaean ocean. *Nat. Geosci.* **2,** 725–729 (2009).
13. Roberson, A. L., Roadt, J., Halevy, I. & Kasting, J. F. Greenhouse warming by nitrous oxide and methane in the Proterozoic Eon. *Geobiology* **9,** 313–320 (2011).
14. Li, Y., Yamaguchi, A., Yamamoto, M., Takai, K. & Nakamura, R. Molybdenum sulfide:
425 A bioinspired electrocatalyst for dissimilatory ammonia synthesis with geoelectrical current. *J. Phys. Chem. C* **121,** 2154–2164 (2017).
15. Halevy, I., Alesker, M., Schuster, E. M., Popovitz-Biro, R. & Feldman, Y. A key role for green rust in the Precambrian oceans and the genesis of iron formations. *Nat. Geosci.* **10,** 135–139 (2017).
430 16. Sorensen, J. & Thorling, L. Stimulation by lepidocrite (7-FeOOH) of Fe(II)-dependent nitrite reduction. *Geochim. Cosmochim. Acta* **55,** 1289–1294 (1991).

17. Hansen, H., Borggaard, O. K. & Sorensen, J. Evaluation of the free energy of formation of Fe(II)-Fe(III) hydroxide-sulphate (green rust) and its reduction of nitrite. *Geochim. Cosmochim. Acta* **58,** 2599–2608 (1994).

435 18. Ottley, C. J., Davison, W. & Edmunds, W. M. Chemical catalysis of nitrate reduction by iron (II). *Geochim. Cosmochim. Acta* **61,** 1819–1828 (1997).

19. Babbin, A. R., Bianchi, D., Jayakumar, A. & Ward, B. B. Rapid nitrous oxide cycling in the suboxic ocean. *Science* **348,** 1127–1129 (2015).

20. Ji, Q., Babbin, A. R., Jayakumar, A., Oleynik, S. & Ward, B. B. Nitrous oxide production
440 by nitrification and denitrification in the Eastern Tropical South Pacific oxygen minimum zone. *Geophys. Res. Lett.* **42,** 10,755–10,764 (2015).

21. Nicholls, J. C., Davies, C. A. & Trimmer, M. High-resolution profiles and nitrogen isotope tracing reveal a dominant source of nitrous oxide and multiple pathways of nitrogen gas formation in the central Arabian Sea. *Limnol. Oceanogr.* **52,** 156–168 (2007).

445 22. Dalsgaard, T., Thamdrup, B., Farías, L. & Revsbech, N. P. Anammox and denitrification in the oxygen minimum zone of the eastern South Pacific. *Limnol. Oceanogr.* **57,** 1331–1346 (2012).

23. Löscher, C. R. *et al.* Production of oceanic nitrous oxide by ammonia-oxidizing archaea. *Biogeosciences* **9,** 2419–2429 (2012).

450 24. Bourbonnais, A. *et al.* N$_2$O production and consumption from stable isotopic and concentration data in the Peruvian coastal upwelling system. *Global Biogeochem. Cycles* **31,** 678–698 (2017).

25. Frame, C. H. & Casciotti, K. L. Biogeochemical controls and isotopic signatures of nitrous oxide production by a marine ammonia-oxidizing bacterium. *Biogeosciences* **7,**
455 2695–2709 (2010).

26. Zafiriou, O. C. & McFarland, M. Nitric oxide from nitrite photolysis in the central equatorial Pacific. *J. Geophys. Res. Atmos.* **86,** 3173–3182 (1981).

27. Liu, C.-Y. *et al.* Determination of dissolved nitric oxide in coastal waters of the Yellow Sea off Qingdao. *Ocean Sci.* **13,** 623–632 (2017).

460 28. Martens-Habbena, W. *et al.* The production of nitric oxide by marine ammonia-oxidizing archaea and inhibition of archaeal ammonia oxidation by a nitric oxide scavenger. *Environ. Microbiol.* **17,** 2261–2274 (2015).

29. Zegeye, A. *et al.* Green rust formation controls nutrient availability in a ferruginous water column. *Geology* **40,** 599–602 (2012).

465 30. Grabb, K. C., Buchwald, C., Hansel, C. M. & Wankel, S. D. A dual nitrite isotopic investigation of chemodenitrification by mineral-associated Fe(II) and its production of nitrous oxide. *Geochim. Cosmochim. Acta* **196,** 388–402 (2017).

31. Gordon, A. D. *et al.* Reduction of nitrite and nitrate on nano-dimensioned FeS. *Orig Life Evol Biosph* **43,** 305–322 (2013).

470 32. Llirós, M. *et al.* Pelagic photoferrotrophy and iron cycling in a modern ferruginous basin. *Sci. Rep.* **5,** 13803 (2015).

33. Swanner, E. D. *et al.* Modulation of oxygen production in Archaean oceans by episodes of Fe(II) toxicity. *Nat. Geosci.* **8,** 126–130 (2015).

34. Sumner, D. Y. Carbonate precipitation and oxygen stratification in late Archean seawater
475 as deduced from facies and stratigraphy of the Gamohaan and Frisco formations, Transvaal Supergroup, South Africa. *Am. J. Sci.* **297,** 455–487 (1997).

35. Sumner, D. Y. & Grotzinger, J. P. Were kinetics of Archean calcium carbonate precipitation related to oxygen concentration? *Geology* **24,** 119 (1996).

36. Battaglia, G. & Joos, F. Marine N_2O emissions from nitrification and denitrification constrained by modern observations and projected in multimillennial global warming simulations. *Global Biogeochem. Cycles* **32,** 92–121 (2018).

37. Hu, R., Seager, S. & Bains, W. Photochemistry in terrestrial exoplanet atmospheres. I. Photochemistry model and benchmark cases. *ApJ* **761,** 166 (2012).

38. Hu, R. & Diaz, H. D. Stability of nitrogen in planetary atmospheres in contact with liquid water. *ApJ* **886,** 1–8 (2019).

39. Wolf, E. T. & Toon, O. B. Fractal organic hazes provided an ultraviolet shield for early Earth. *Science* **328,** 1266–1268 (2010).

40. Kaiser, J., Röckmann, T., Brenninkmeijer, C. A. M. & Crutzen, P. J. Wavelength dependence of isotope fractionation in N_2O photolysis. *Atmos. Chem. Phys.* **3,** 303–313 (2003).

41. Airapetian, V. S., Glocer, A., Gronoff, G., Hebrard, G. & Danchi, W. Prebiotic chemistry and atmospheric warming of early Earth by an active young Sun. *Nat. Geosci.* **9,** 452–455 (2016).

42. Catling, D. C., Zahnle, K. J. & McKay, C. P. Biogenic methane, hydrogen escape, and the irreversible oxidation of early Earth. *Science* **293,** 839–843 (2001).

43. Laneuville, M., Kameya, M. & Cleaves, H. J., II. Earth without life: A systems model of a global abiotic nitrogen cycle. **18,** 897–914 (2018).

44. Saito, M. A. *et al.* Abundant nitrite-oxidizing metalloenzymes in the mesopelagic zone of the tropical Pacific Ocean. *Nat. Geosci.* **13,** 355–362 (2020).

45. Summers, D. P. & Chang, S. Prebiotic ammonia from reduction of nitrite by iron (II) on the early Earth. *Nature* **365,** 630–633 (1993).

46. Brandes, J. A. *et al.* Abiotic nitrogen reduction on the early Earth. *Nature* **395,** 365–367 (1998).

47. Nishizawa, M. *et al.* Stable abiotic production of ammonia from nitrate in komatiite-hosted hydrothermal systems in the Hadean and Archean oceans. *Minerals* **11,** 1–30 (2021).

48. Laneuville, M., Kameya, M. & II, H. J. C. Earth without life: A systems model of a global abiotic nitrogen cycle. *Astrobiology* **18,** 897–914 (2018).

49. Halevy, I. & Bachan, A. The geologic history of seawater pH. *Science* **355,** 1069–1071 (2017).

50. Harman, C. E. *et al.* Abiotic O_2 levels on planets around F, G, K, and M stars: Effects of lightning-produced catalysts in eliminating oxygen false positives. *ApJ* **866,** 56 (2018).

51. Mather, T. A., Pyle, D. M. & Allen, A. G. Volcanic source for fixed nitrogen in the early Earth's atmosphere. *Geology* **32,** 905–908 (2004).

52. Kasting, J. F. Bolide impacts and the oxidation state of carbon in the Earth's early atmosphere. *Orig Life Evol Biosph* **20,** 199–231 (1990).

53. Ducluzeau, A.-L. *et al.* Was nitric oxide the first deep electron sink? *Trends Biochem. Sci.* **34,** 9–15 (2009).

54. Viebrock, A. & Zumft, W. G. Molecular cloning, heterologous expression, and primary structure of the structural gene for the copper enzyme nitrous oxide reductase from denitrifying *Pseudomonas stutzeri*. *J. Bacteriol.* **170,** 4658–4668 (1988).

55. Chen, J. & Strous, M. Denitrification and aerobic respiration, hybrid electron transport chains and co-evolution. *Biochim. Biophys. Acta Bioenerg.* **1827,** 136–144 (2013).

56. Suharti & de Vries, S. Membrane-bound denitrification in the Gram-positive bacterium *Bacillus azotoformans*. *Biochem. Soc. Trans.* **33,** 130–133 (2005).

57. Saraste, M. & Castresana, J. Cytochrome oxidase evolved by tinkering with denitrification enzymes. *FEBS Letters* **341,** 1–4 (1994).

58. Sousa, F. L. *et al.* The superfamily of heme–copper oxygen reductases: Types and evolutionary considerations. *Biochim. Biophys. Acta Bioenerg.* **1817,** 629–637 (2012).

59. Chen, J. & Strous, M. Denitrification and aerobic respiration, hybrid electron transport chains and co-evolution. *Biochim. Biophys. Acta Bioenerg.* **1827,** 136–144 (2013).

60. Yoon, S. *et al.* Nitrous oxide reduction kinetics distinguish bacteria harboring clade I NosZ from those harboring clade II NosZ. *Appl. Environ. Microbiol.* **82,** 3793–3800 (2016).

61. Babbin, A. R., Bianchi, D., Jayakumar, A. & Ward, B. B. Rapid nitrous oxide cycling in the suboxic ocean. *Science* **348,** 1127–1129 (2015).

62. Heinrich, T. A. *et al.* Biological nitric oxide signalling: chemistry and terminology. *Br. J. Pharmacol.* **169,** 1417–1429 (2013).

63. Santana, M. M., Gonzalez, J. M. & Cruz, C. Nitric Oxide Accumulation: The Evolutionary Trigger for Phytopathogenesis. *Front. Microbiol.* **8,** 267 (2017).

64. Nikeleit, V. *et al.* Inhibition of photoferrotrophy by nitric oxide in ferruginous environments. *Earth ArXiv* 1–63 (2021). doi:10.31223/X5XS60

65. Drummond, J. T. & Matthews, R. G. Nitrous oxide degradation by cobalamin-dependent methionine synthase: Characterization of the reactants and products in the inactivation reaction. *Biochemistry* **33,** 3732–3741 (1994).

66. Drummond, J. T. & Matthews, R. G. Nitrous oxide inactivation of cobalamin-dependent methionine synthase from *Escherichia coli*: Characterization of the damage to the enzyme and prosthetic group. *Biochemistry* **33,** 3742–3750 (1994).

67. Matthews, R. G. Cobalamin-dependent methyltransferases. *Accounts of Chemical Research* **34,** 681–689 (2001).

68. Buessecker, S. *et al.* Microbial communities and interactions of nitrogen oxides with methanogenesis in diverse peatlands of the Amazon basin. *Front. Microbiol.* **12,** 1–15 (2021).

69. McDonnell, A. M. P. & Buesseler, K. O. Variability in the average sinking velocity of marine particles. *Limnol. Oceanogr.* **55,** 2085–2096 (2010).

70. Krissansen-Totton, J., Olson, S. & Catling, D. C. Disequilibrium biosignatures over Earth history and implications for detecting exoplanet life. *Sci. Adv.* **4,** eaao5747 (2018).

Methods

565   *Mineral synthesis*. Carbonate green rust was synthesized according to the following. In brief, 18.2

MΩ·cm water was made anoxic by boiling and sparging with CO_2/N_2 (20:80). An anoxic 0.4 M

Fe^{2+}/Fe^{3+} solution (0.1 L) was prepared by mixing 7.42 g of $FeSO_4 \times 7\ H_2O$ (>99%, Sigma Aldrich)

and 2.66 g of anhydrous $Fe_2(SO_4)_3$ (97%, Sigma Aldrich). An alkaline, anoxic solution of 0.466 M

Na_2CO_3 (Fisher Scientific) in 0.8 M NaOH (Fisher Scientific) (0.1 L) was prepared by dissolving

570   NaOH first under a constant stream of CO_2/N_2 gas, after which Na_2CO_3 was added. Both solutions

were stirred continuously at 500 rpm. The alkaline solution was injected into the Fe^{2+}/Fe^{3+} solution

using CO_2/N_2 flushed syringes. Precipitation occurred immediately and the suspension was stirred

in the dark for 24 hours. Magnetite was synthesized as nanoparticles following previously

described protocols[71,72].

575

  Mineral harvest. Green rust and magnetite precipitates were washed in an anaerobic chamber

(0.5% H_2 in N_2, Coy Laboratory Products) using a vacuum filtration unit (Nalgene, Mfr # 130-

4020) and 0.45 μm cellulose-acetate filter membranes (Sartorius). Anoxic 18.2 MΩ·cm water was

poured onto the precipitates for a minimum of 8 cycles (pouring followed by extracting water).

580   When filtrate flow ceased to a minimum, the wet mineral paste was removed from the filter. Wet

carbonate green rust (73.8% water content) and wet magnetite (47.2% water content) were added

to microcosms. The wet minerals were also used for mineralogical characterization (XRD and

microscopy). For BET analysis, a defined amount of precipitate was dried in small boxes filled

with drierite and placed into the anaerobic chamber. Dry weight was constant after 3-5 days.

585

X-ray diffractometry (XRD). Powder X-ray diffractometry was conducted on a subset of samples

after synthesis and washing of the mineral products. A glycerol smear was prepared with 10 mg

sample in the anaerobic chamber and sealed in a glass vial to prevent oxidation prior to analysis.

To collect the XRD data, the sample was removed from the vial and spread across a quartz zero

590 background plate that was placed onto a horizontal stage in a Bruker D-5000 diffractometer

(Bruker, Germany) equipped with a Co Kα X-ray tube (30 kV, λ = 1.791Å). Signal peaks were

compared to reference diffractograms in the RRUFF database. Instrument broadening was

determined by a standard polycrystalline alumina sample. X-ray diffractometry data was analyzed

with the CrystalDiffract software version 6.8.2 for Mac.

595

Scanning- and transmission-electron microscopy (SEM, TEM). Samples for SEM imaging were

mounted on aluminum pin stubs with double-sided carbon tabs in the glove box and transported in

a sealed jar with anoxic atmosphere to the microscope. Samples were not sputter-coated. Images

were taken on an XL30 ESEM-FEG (Philips) operated at a 30 kV accelerating voltage and a 21 pA

600 beam current. TEM samples were dispersed on a Lacey Carbon film using 200 mesh copper grids.

The instrument used was a CM200 Field Emission Microscope at 200KV (Philips) with C_s = 1.2

mm and a PTP resolution of 0.25 nm. Imaging was done on a Gatan Orius CCD system.

Brunauer-Emmett-Teller (BET) surface area measurements. For analysis of the BET surface area,

605 dried mineral precipitate was weighed inside the anaerobic chamber and added to a Florence glass

flask that was closed with a rubber stopper for transport to the instrument. BET surface in replicate

samples (n = 3 for GR, n = 2 for magnetite) was quantified using N_2 gas on a Tristar II 3020

analyzer (Micromeritics Inc.). The instrument has a limit of detection of 1 m^2. Our results

(*Supplementary Table 4*) are roughly consistent with previously determined BET values of 47 m^2 g^{-1} for GR[73] and 95 m^2 g^{-1} for magnetite[74].

We performed calculations of the mineral surface area for both minerals to supplement our measurements. To derive the mineral density, we calculated the average crystallite size by inserting the full width at half maximum, as determined from the diffractograms and the Bragg angle of the GR 0 0 3 reflection and of the magnetite 3 1 1 reflection, into the Scherrer equation. Mineral density was calculated using the formula $\rho = (M \times Z)/(V_c \times 0.60225)$ where M is molar mass, Z is the number of molecules per crystallite and V_c is crystallite size. The density and the grain volume as measured by TEM/SEM were used to calculate the grain mass. The final value in m^2 g^{-1} was derived from the grain mass and the grain surface area (TEM/SEM). For magnetite, we calculated a surface area of 88.8 m^2 g^{-1}. For green rust, we calculated a minimum approximation (surface of green rust sheets only) of 27.6 m^2 g^{-1} and a maximum approximation (including surface between sheets) of 538.5 m^2 g^{-1}. Thus, our measured value for magnetite is somewhat lower than the calculated and literature value. The measured value for green rust is in good agreement with the literature value and at the lower end of the calculated range.

Incubation conditions. Interactions of nitrogen oxides with Fe minerals were tested in anoxic microcosms designed to mimic Archean ocean conditions as closely as possible. Borosilicate glass bottles (30-120 mL) were closed with thick butyl rubber stoppers and a headspace of 20% CO_2 in N_2 was used throughout the experiment. All glassware was washed with 2 M HCl prior to use. The liquid phase constituted one third of the microcosm total volume. We used a published recipe for artificial Archean seawater[75] and omitted any sulfur species (0.56 M NaCl, 0.01 M NaHCO$_3$). The pH was initially set to 7.3 using a CO_2–HCO_3^- buffer. We boiled 18.2 MΩ·cm water and sparged it

with CO_2/N_2 (20:80) while it was cooling on ice. Salts were added during the sparging. The anoxic

solution was then dispensed with a pipetor into microcosms in an anaerobic chamber (0.5% H_2 in

N_2, Coy Laboratory Products). Nitrate and nitrite stock solutions were prepared with their

635 respective sodium salts $NaNO_3$ (≥99%, Fisher Scientific) and $NaNO_2$ (≥97%, Acros Organics) and

dissolved in artificial seawater. The solutions were then sparged with N_2 and filter-sterilized

(0.8/0.2 µm pore seize, VWR) in the anaerobic chamber. Controls with aqueous Fe^{2+} were

prepared in anoxic artificial seawater and $FeCl_2$ (≥99%, Fisher Scientific). Mineral surface area

was controlled by the mineral mass added. Wet minerals were weighed in the anaerobic chamber

640 and distributed into microcosms using ethanol-washed plastic spatulas. Prior to start of the

incubations with the injection of the NO_x^- solution, mineral agglomerates were dissipated in an

ultrasonic bath (Ultrasonic cleaner 2510, Branson Ultrasonics). Microcosms were shaken at 250

rpm in the dark and at room temperature over the whole duration of the experiment. Controls were

incubated in the anaerobic chamber to test for potential leaking through stoppers, which did not

645 occur. To dissolve mineral particles during incubations, 1.6 mL of concentrated 12N HCl or 37N

H_2SO_4 was slowly injected through bottle septa to 10 mL mineral-seawater suspension.

Dissolution of solid particles occurred instantly and the liquid first turned turbid orange-green and

then clear green-yellow (HCl) or light yellow (H_2SO_4) within 15-20 hours. The last measurement

of NO in the headspace was taken when the liquid was clear (*Supplementary Fig. 5*).

650

Dissolved nitrite, nitrate, ammonium, ferrous and ferric iron measurements. All dissolved analytes

were quantified spectrometrically with plate assays. Nitrite in solution was quantified with the

Griess reagent (Promega, Kit G2930). Nitrate was first reduced to nitrite by vanadium(III) chloride

and then quantified as nitrite[76]. Ammonium production was verified with the salicylic acid assay[77].

655 To determine the Fe^{2+}/Fe^{3+} solid phase ratio, mineral particles were settled, after which supernatant artificial seawater was removed from the microcosms. Anoxic acidic extraction of green rust and magnetite was conducted by completely dissolving mineral samples in 6 M HCl, followed by incubation at 70 °C for 24 hours under 100% N_2 headspace to prevent abiotic oxidation[71]. The samples were then further diluted 1:10 in 1 M HCl. Ferrous and ferric ions in the extracts were

660 measured by reaction with ferrozine after the method of Stookey[78].

N_2O gas measurements. To quantify N_2O production, 200 μL of headspace gas was sampled with a gas-tight syringe (VICI Precision Sampling) and injected into a gas chromatograph (GC, SRI Instruments) equipped with an electron-capture detector (ECD). Two continuous HayeSep-D

665 columns were kept at 90°C (oven temperature) and N_2 (UHP grade 99.999%, Praxair Inc.) was used as carrier gas. The ECD current was 250 mV and the ECD cell was kept at 350°C. The N_2O measurements were calibrated using customized standard mixtures (Scott Specialty Gases, accuracy ±5%) over a range of 0.25–100 ppmv. Gas accumulation in the microcosms was monitored over time. Gas concentrations were corrected using Henry's law and the dimensionless

670 concentration constant $k_H{}^{cc}(N_2O) = 0.6112$ to account for gas partitioning into the aqueous phase at 25°C.

NO gas measurements. Nitric oxide (NO) was quantified in the microcosm headspace with a chemiluminescence-based analyzer (LMA-3D NO_2 analyzer, Unisearch Associates Inc.).

675 Headspace gas (50 μL) was withdrawn with a CO_2-N_2-flushed gas-tight syringe and injected into the analyzer. The injection port was customized to fit the injection volume and consisted of a T-junction with an air filter at one and a septum at the other end. An internal pump generated

consistent airflow. In short, sample NO was oxidized to NO_2 by a CrO_3 catalyst. The NO_2 flew

across a fabric wick saturated with a Luminol solution. Luminol was obtained from Drummond

680   Technology Inc. (Canada). Readings were corrected for background NO_2 every 15 minutes

("zeroing"). Shell airflow rate was kept at 500 mL min^{-1} and the span potentiometer was set to 8.

Measurements were calibrated with a 0.1 ppm NO (in N_2) standard (<0.0005 ppm NO_2, Scott-

Marin Inc.) over a range of 5–1,000 ppbv. Gas concentrations were corrected using Henry's law

and the dimensionless concentration constant $k_H{}^{cc}(NO) = 0.0465$ to account for gas partitioning

685   into the aqueous phase at 25°C.

Flux modeling. The partial fluxes of the overall flux balance $\Phi_{sed} + \Phi_{par} = \Phi_{atm}$ were normalized to

a 100 m vertical slab with 1 m^2 basis. The upper 100 m ocean water are typically considered as

well-mixed, hence, reactant and catalyst are homogeneously distributed in that space. Depending

690   on the water depth, a portion of the NO_x could reach the ocean floor, which is why we added a

generic sediment flux (Φ_{sed}) to the balance equation. The dominant flux would emerge from

floating GR mineral particles (Φ_{par}) that are distributed along the water column. For simplicity, we

assume that all GR had aged into magnetite in the sediment and all floating particles were GR

phases. We refer to the *Supplementary Information* for a more detailed description of the

695   derivation of the partial fluxes, the error propagation method, and thermodynamic calculations.

Photochemical modeling. We have used an atmospheric photochemistry model to simulate the

effects of N_2O emission into an anoxic atmosphere akin to the Archean Earth's condition. The

photochemistry model used[37,79] has been validated by computing the atmospheric compositions of

700   present-day Earth and Mars, as the outputs agreed with the observations of major trace gases in

Earth's and Mars' atmospheres[80]. For example, Figure 2-2 of ref. [80] shows that the model reproduces the vertical profile of the mixing ratio of N_2O in modern Earth's atmosphere using a globally averaged emission rate (1×10^9 molecules cm^{-2} s^{-1}). For this work, we simulate a 1-bar atmosphere of 95% N_2 and 5% CO_2 to approximate the anoxic and CO_2-rich environment of the Archean Earth[81]. We have used the UV and optical spectrum of the present-day Sun to drive the photochemical model because the solar flux in 200-230 nm, which causes the photodissociation of N_2O, depends weakly on the age[82]. We have updated the absorption cross sections of CO_2 and H_2O using the latest experimental results[83]. We assume a surface temperature of 288 K and a stratospheric temperature of 200 K, and adopt the eddy diffusion coefficient derived from the number density profiles of trace gases on Earth[84]. The photochemistry model includes a comprehensive reaction network for O, H, C, N, and S species including sulfur and sulfuric acid aerosols, and includes volcanic outgassing of CO, H_2, SO_2, and H_2S. The outgassing rate is not high enough to produce a H_2SO_4 aerosol layer in the atmosphere and these gases do not impact the lifetime of N_2O significantly.

Data availability

All data are provided in the manuscript and the supplementary materials, and are available as raw data on the figshare platform (https://doi.org/10.6084/m9.figshare.20740204.v2) or upon request from the authors.

Code availability

The code for the photochemical model will be shared by the authors upon request.

725

Methods-only References

71. Byrne, J. M. *et al.* Redox cycling of Fe(II) and Fe(III) in magnetite by Fe-metabolizing bacteria. *Science* **347,** 1473–1476 (2015).

730 72. Pearce, C. I. *et al.* Synthesis and properties of titanomagnetite ($Fe_{3-x}Ti_xO_4$) nanoparticles: A tunable solid-state Fe(II/III) redox system. *J. Colloid Interface Sci.* **387,** 24–38 (2012).

73. Williams, A. G. B. & Scherer, M. M. Kinetics of Cr(VI) reduction by carbonate green rust. *Environ. Sci. Technol.* **35,** 3488–3494 (2001).

74. Sun, Z.-X., Su, F.-W., Forsling, W. & Samskog, P.-O. Surface characteristics of magnetite

735 in aqueous suspension. *J. Colloid Interface Sci.* **197,** 151–159 (1998).

75. Anbar, A. D. & Holland, H. D. The photochemistry of manganese and the origin of banded iron formations. *Geochim. Cosmochim. Acta* **56,** 2595–2603 (1992).

76. Miranda, K. M., Espey, M. G. & Wink, D. A. A Rapid, Simple Spectrophotometric Method for Simultaneous Detection of Nitrate and Nitrite. *Nitric Oxide* **5,** 62–71 (2001).

740 77. Kandeler, E. & Gerber, H. Short-term assay of soil urease activity using colorimetric determination of ammonium. *Biol Fertil Soils* **6,** 68–72 (1988).

78. Stookey, L. L. Ferrozine – a new spectrophotometric reagent for iron. *Anal. Chem.* **42,** 779–781 (1970).

79. Hu, R., Seager, S. & Bains, W. Photochemistry in Terrestrial Exoplanet Atmospheres. II.

745 H_2S and SO_2 Photochemistry in Anoxic Atmospheres. *ApJ* **769,** 1–6 (2013).

80. Hu, R. Atmospheric photochemistry, surface features, and potential biosignature gases of terrestrial exoplanets. Thesis (2013).

81. Catling, D. C. & Zahnle, K. J. The Archean atmosphere. *Sci. Adv.* **6,** eaax1420 (2020).

82. Claire, M. W. *et al.* The evolution of solar flux from 0.1 nm to 160 μm: Quantitative

750 estimates for planetary studies. *ApJ* **757,** 95 (2012).

83. Ranjan, S. *et al.* Photochemistry of anoxic abiotic habitable planet atmospheres: Impact of new H_2O cross sections. *ApJ* **896,** 148 (2020).

84. Massie, S. T. & Hunten, D. M. Stratospheric eddy diffusion coefficients from tracer data. *J. Geophys. Res. Atmos.* **86,** 9859–9868 (1981).

755